THE JOURNAL OF PHYSICAL CHEMISTRY C
A JOURNAL OF THE AMERICAN CHEMICAL SOCIETY

pubs.acs.org/JPCC

Article

Understanding Oligonucleotide Hybridization and the Role of Anchoring on the Single-Walled Carbon Nanotube Corona Phase for Viral Sensing Applications

Jianqiao Cui,[#] Xun Gong,[#] Soo-Yeon Cho, Xiaojia Jin, Sungyun Yang, Roya Khosravi-Far, and Michael S. Strano*

Cite This: *J. Phys. Chem. C* 2023, 127, 606−620

Read Online

ACCESS | Metrics & More | Article Recommendations | Supporting Information

ABSTRACT: Semiconducting single-walled carbon nanotubes (SWCNTs) with tailored corona phases (CPs), or surface-adsorbed molecules, have emerged as a promising interface for sensing applications. The adsorption of an analyte can be specifically transduced as a modulation of their band-gap near-infrared (nIR) photoluminescence (PL). One such CP ideal for this purpose is single-stranded DNA (ssDNA), where subsequent sequence-dependent hybridization can result in PL emission wavelength shifts. Due to ssDNA adsorption to the SWCNT surface, the resultant noncanonical hybridization and its effect on SWCNT photophysical properties are not well understood. In this work, we study 20- and 21-mer DNA and RNA hybridization on the complementary ssDNA-SWCNT CP in the context of nucleic acid sensing for SARS-CoV-2 sequences as model analytes. We found that the van't Hoff transition enthalpy of hybridization on SWCNT CP was −11.9 kJ mol^{-1}, much lower than that of hybridization in solution (−707 kJ mol^{-1}). We used SWCNT solvatochromism to calculate the solvent-exposed surface area to indicate successful hybridization. We found that having a 30-mer anchor region in addition to the complementary region significantly improved PL response sensitivity and selectivity, with a $(GT)_{15}$ anchor preferred for RNA targets. Coincubation of ssDNA-SWCNTs with an analyte at 37 °C resulted in faster hybridization kinetics without sacrificing specificity. Other methods aimed to improve CP rearrangement kinetics such as bath sonication and surfactant additions were ineffective. We also determined that the target sequence choice is important as secondary structure formation in the target is negatively correlated with hybridization. Best-performing CPs showed detection limits of 11 and 13 nM for DNA and RNA targets, respectively. Finally, we simulated sensing conditions using the saliva environment, showing sensor compatibility in biofluids. In total, this work elucidates key design features and processing to enable sequence-specific hybridization on ssDNA-SWCNT CPs.

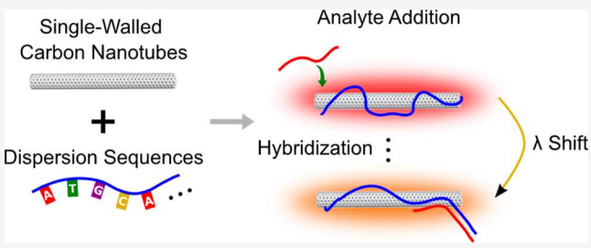

INTRODUCTION

Detection of single-stranded oligonucleotides through complementary hybridization plays an essential role in diagnostic pathology,[1,2] drug discovery and delivery,[3,4] and molecular biology.[5,6] In the case of biosensing, materials with unique nanoscale properties were often used as scaffolds for single-stranded DNA (ssDNA) immobilization to construct probe or transducer elements,[7] with specificity arising from hybridization at the solid−liquid nanomaterial interface. For these constructs, interfacial traits including surface strand density,[8−12] surface charge,[13−15] substrate porosity,[16] point mismatch,[17−19] immobilized DNA length,[20] brush effect for long targets,[21] and probe attachment chemistry[22−24] have been shown to influence hybridization stability and kinetics. While initial studies involved flat microchip arrays, nanomaterials such as gold nanoparticles[22,25−28] and carbon nanotubes[29−32] revealed unique interfacial properties potentially useful for sensor design. Such nanomaterial surfaces often entail constrained probe conformations that result in noncanonical hybridization behaviors that are not as well studied, motivating our current study.

A large fraction of current DNA-nanomaterial hybrid studies utilize carbon-based substrates.[33−37] Of them, semiconducting single-walled carbon nanotubes (SWCNTs) have advantages as sensor components, particularly due to their photophysical properties.[38,39] Small-diameter SWCNTs are favorable for biomedical applications because of their photoluminescence (PL) emissions at near-infrared (nIR) wavelengths,[40] where there is minimal optical absorption from blood and tissue[41−43] as well as cellular autofluorescence.[44] Additionally, SWCNTs

Received: September 8, 2022
Revised: November 16, 2022
Published: December 27, 2022

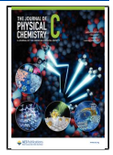

are resistant to photobleaching[45,46] compared to conventional fluorescent dyes, allowing for long-term temporal monitoring of fluorescence signals.[46,47] Furthermore, SWCNTs can be engineered to form specifically tailored and stable corona phases (CPs),[48] or noncovalent wrappings, in aqueous environments for specific analyte recognition with up to single-molecule sensitivity.[49,50] When a target analyte binds to the SWCNT corona, the perturbation introduced to the local environment can be transduced via changes in the SWCNT fluorescence signal in the form of modulations in their emission wavelength[51] and/or intensity.[52]

The ssDNA-SWCNT CPs have been explored recently as hybridization sensors against DNA (ssDNA),[53] microRNA,[31] and viral RNA targets.[32,54] These sensors report local target analyte concentrations in the form of PL emission wavelength shifts. Some studies have included noncomplementary ssDNA regions within the CP to improve hybridization signal transduction, the theory being that having "anchor" regions will allow for increased solution-phase analyte interactions.[55] Although these anchor regions have shown promise, their design is not well understood. Furthermore, it is well known that ssDNA as part of the SWCNT CP behaves noncanonically, making hybridization efficacy sequence-dependent. Nevertheless, complementary sequences have been shown to be correlated with CP reorganization, as demonstrated by atomic force microscopy of 30-mer oligonucleotides.[56] However, differences between CP sequences prompt a systematic study of the ssDNA-SWCNT hybridization process to enable a directed search of sensor candidates.

In this work, we used tailored SARS-CoV-2 complement sequences to understand the tunable parameters in ssDNA-SWCNT CP hybridization sensor design. By measuring the kinetics of the hybridization process, we calculated and compared its enthalpy to solution-phase hybridization. By using a SWCNT diameter-dependent solvatochromism model, we correlated observed photophysical changes to the CP changes and solvent-exposed surface area following hybridization. We also definitively demonstrated that PL response specificity can be improved through the inclusion of anchor sequences, with anchor-absent SWCNT CPs showing no specificity. We also systematically studied the anchor sequence and location configurations to result in multiple promising candidates for both DNA and RNA targets. Target sequence choice was found to be a significant factor in hybridization and signal transduction. Finally, we demonstrated these sensor candidates in biologically relevant testing conditions. Our work represented a comprehensive investigation into the mechanism of hybridization of complementary sequences on the SWCNT corona. Developing these methods and understanding them is a significant step toward developing a new generation of hybridization sensors enabled by the ssDNA-SWCNT platform.

MATERIALS AND METHODS

Materials. Raw CoMoCAT SWCNTs enriched in (6,5) chirality were purchased from Sigma-Aldrich and used without further processing (Lot # MKCM1708). Single-strand DNA and RNA oligonucleotides were purchased from Integrated DNA Technologies. All other chemicals were purchased from Sigma Millipore.

Target Viral RNA Sequence Design. Sequences were chosen intuitively with the aid of software tools. UNAFold Software was used, which is a common folding algorithm that predicts nucleic acid foldings, hybridizations, and melting profiles using energy-based methods and dynamic programming.[57] We identified regions longer than 18 nucleotides that are predicted to be exposed with minimal secondary structure formation based on the SARS-CoV-2 genome. We further BLAST-searched them to show 100% identity with their designated gene for SARS-CoV-2 and specificity against OC43, 229E, NL63, MERS, and SARS1 coronaviruses, as well as any gene in the human genome.

Nanosensor Preparation and Characterization. 1 mg of CoMoCAT SWCNT and 1 mg of ssDNA were mixed in 1 mL of 100 mM NaCl. The mixture was ultrasonicated with a 1/8″ probe tip (Cole-Parmer) for 30 min at 44% amplitude in an ice bath. The sample was then centrifuged twice at 30,300*g* for 1 h (Eppendorf Centrifuge 5430R). After each centrifugation, the top 80% of the suspension was collected, while the remaining 20% was discarded to remove unsuspended bundles. The centrifuged sample was dialyzed against phosphate-buffered saline (PBS) with a 1 mL dialysis device of 300 kDa MWCO (Spectra-Por) overnight to remove free DNA. The concentration of the SWCNT suspension was determined using its absorbance at 632 nm (Agilent Technologies, Cary 5000) and extinction coefficient of 0.036 mg L^{-1} cm^{-1}. The sample was stored at 4 °C in a fridge for further use.

High-Throughput Screening and nIR PL Spectrum Processing. High-throughput screening of the nanosensor library against the viral nucleotides was performed using a customized nIR microscope, which consists of a Zeiss Axio Vision inverted microscope body with a 20× objective, coupled to an Acton SP2500 spectrometer and liquid nitrogen-cooled InGaAs 1D detector (Princeton Instruments). The dialyzed SWCNT dispersion was diluted to 0.5 mg L^{-1} and allowed to equilibrate overnight at room temperature before hybridization experiments. For screening, a 50 μM stock solution of each target oligonucleotide in PBS was prepared. In a 96-well plate, 200 μL of SWCNT dispersion (0.5 mg L^{-1}) was added to 2 μL of a 50 μM oligonucleotide solution. The addition of 2 μL of PBS was used as a negative control. The mixture was incubated for 1 h at 37 °C, after which the SWCNT fluorescence signal was monitored under laser excitation (785 nm, 317 mW, B&W Tek Inc). The fluorescence spectra from three replicates were collected from 950 to 1250 nm. Following the acquisition, the spectra were processed in a custom MATLAB code which interpolates the spectra to locate the peak wavelength. (6,5), (7,5), and (9,4) chiralities were assigned to the peaks at circa 990, 1045, and 1128 nm, respectively. The (7,5) and (9,4) peak wavelengths were obtained by subtracting the influences of nearby chiralities. Specifically, the spectral shoulders present near the (7,5) and (9,4) peaks were cropped out by subtracting a fourth-order polynomial fit of the surrounding regions. The peak wavelengths of each sensor−nucleotide pair were then compared to that of the sensor−PBS negative control to calculate the wavelength shift.

Hybridization Experiments with Surfactants, Biofluids, and Bath Sonication. Hybridization experiments were conducted with a 0.5 mg L^{-1} SWCNT dispersion and target DNA or RNA at a final concentration of 500 nM unless otherwise stated in the titration experiments in Figure 5. Bath sonication was carried out using a 110 V ultrasonic bath (Arrayit Corporation). In these experiments, target DNA or RNA was first introduced to the SWCNT dispersion, followed by bath sonication, and then 1 h incubation at the specified

https://doi.org/10.1021/acs.jpcc.2c06434
J. Phys. Chem. C 2023, 127, 606−620

temperature in Figure 4 or 1 h incubation and then bath sonication. Hybridization experiments with a surfactant were carried out at the final concentrations specified in Figure 4. The surfactant solution was added to the SWCNT dispersions either at the same time as the addition of target DNA or 12 h before the addition of the target oligonucleotide. Regardless, the mixtures were incubated at 37 °C for 1 h before their fluorescence spectra were acquired. The saliva sample was sourced from pooled human donors (MyBioSource) and was introduced to the SWCNT dispersion at a final concentration of 1% v/v. Spectra were acquired after 1 h of incubation at 37 °C.

RESULTS AND DISCUSSION

Construct Synthesis, Design Study, and Measurement Conditions. Nucleic acids are well known to form stable CPs around SWCNTs in aqueous environments via $\pi-\pi$ stacking between the nucleoside and the SWCNT surface with the negatively charged phosphate backbones acting as the hydrophilic solution-facing components.[58−60] The adsorbed ssDNA on the SWCNT surface can bind to the complementary oligonucleotides introduced to the solution and result in a measurable wavelength modulation of the SWCNT PL. ssDNA-SWCNT constructs were synthesized using the raw SWCNT material from the CoMoCAT process, enriched with the (6,5) chirality species. A standard solution-phase sonication method was used to disperse the SWCNTs against a specifically designed library of ssDNA oligonucleotides with complementary components to the 11 segments of the SARS-CoV-2 viral RNA genome (Table 1). Briefly, the ssDNA-SWCNT dispersions were created by ultrasonicating mixtures of ssDNA and CoMoCAT SWCNT in a 100 mM NaCl solution, followed by centrifugation to remove SWCNT aggregates and dialysis with 1× PBS buffer overnight to remove excess unbound ssDNA from the solution. The concentration of the DNA-SWCNT dispersion was determined using the typical method of absorbance at 632 nm with an extinction coefficient of 0.036 L mg^{-1} cm^{-1}.[61]

Table 1. Target Sequences from SARS-CoV-2 for Detection with the ssDNA-SWCNT Construct

target	sequences (5′ → 3′)	gene encoding
S1712	ACACTACTGATGCTGTCCGT	spike (S) protein
S3555	CCTCAATGAGGTTGCCAAGA	spike (S) protein
N158	TCACCGCTCTCACTCAACAT	nucleocapsid (N) protein
N563	CACGTAGTCGCAACAGTTCA	nucleocapsid (N) protein
M296	CTTTCAGACTGTTTGCGCGT	membrane (M) protein
M566	GTGACTCAGGTTTTGCTGCA	membrane (M) protein
E160	CCTTCTTTTTACGTTTACTCT	envelope (E) protein
E198	TTCTTCTAGAGTTCCTGATC	envelope (E) protein
O1256	AGTGTGCCTATTGGGTTCCA	ORF 1-ab
O6736	TCAACCGCTGCTTTAGGTGT	ORF 1-ab
O10098	TGTTCGCATTCAACCAGGAC	ORF 1-ab

RNA secondary structures play a key role in affecting complementary hybridization. Predicting the secondary structure of RNA has long been studied to facilitate many genomics applications.[62,63] In order to design sensors that can efficiently interact with the SARS-CoV-2 genes, we used a combination of software and manual alignment for identifying RNA genome regions that are predicted to be the exposed regions of the spike (S), nucleocapsid (N), membrane (M), envelope (E), and open-reading frame (ORF) of SARS-CoV-2 genes. Some of the sequence design considerations include specificity to the target of interest and the minimization of secondary structures. The guanine−cytosine (GC) content of the sequences was also ensured to be evenly distributed to minimize hairpin and self-binding. Using this strategy, 11 unique sequences for the S, N, M, and E genes and the ORF of the SARS-CoV-2 virus (Table 1) were selected.

PBS was chosen to constitute a physiologically relevant but also buffered environment to reduce readout variability. Additional precautions were taken to improve measurement fidelity, including diluting ssDNA-SWCNT to 0.5 mg/L to reduce aggregation, equilibrating SWCNT dilutions overnight, exciting the solution at a low laser fluence (1.78×10^4 mW/cm^2), and mixing well during analyte incubation at a consistent temperature.[64]

For each hybridization experiment, the DNA or RNA analyte was mixed with the SWCNT at a final concentration of 500 nM. Analytes can be complements to the ssDNA wrapping (cDNA and cRNA), randomly generated noncomplementary control sequences (nDNA and nRNA), or PBS buffer. For clarity, ssDNA strands within the CP will be referred to as "adsorbed" and solution-phase testing strands referred to as the "analyte". The mixture was then incubated under a chosen experimental condition before the PL spectra were acquired in the 850−1250 nm range at approximately 2.56 pixel/nm using a high-throughput custom-made nIR fluorescence microscope. To extract the SWCNT PL peak wavelength at subpixel resolutions, using the 990 nm peak as an example, a Gaussian function was fit over data points near 990 nm to obtain the PL peak wavelength. The peak position after analyte incubation was compared to that of the PBS control to calculate wavelength shifts.

Kinetics and Thermodynamics of SWCNT Surface Hybridization. In a typical experiment, we expected that the ssDNA-SWCNT PL peak would shift after coincubation with the complementary analyte, while it would remain unchanged after coincubation with the noncomplementary analyte (Figure 1b). This observation is attributed to solvatochromism,[51] where a shift in the optical transition energy, called the solvatochromic shift, results from a change in the exciton polarizability of the SWCNT due to changes in its local dielectric environments (solvent Stark effect). The magnitude of this shift has been shown to scale approximately to the −4 power with the SWCNT diameter (d^{-4}) and with the square of the transition energy (E_{ii}^2).[51] A hypsochromic shift, or an increase in electronic transition energy, indicates a decrease in the effective dielectric constant of the SWCNT local environment. In this context, when the CP adsorbs more densely at the SWCNT surface, high-dielectric-constant water is excluded, causing the measured hypsochromic shift. In this way, a bathochromic shift (to the red or lower energy) conversely indicates a looser packing or lower density of the SWCNT corona.[53]

For an adsorbed analyte pair with a known response, we used the temporal changes of SWCNT PL (Table S1) at 24, 37, and 50 °C to first study the kinetics of the process. At all temperatures, we observed an increasing hypsochromic shift followed by cDNA addition and a negligible change followed by nDNA addition (Figure 1c). This selectivity suggests that hybridization plays a role. Nearly 20 h and 10 h were needed to

https://doi.org/10.1021/acs.jpcc.2c06434
J. Phys. Chem. C 2023, 127, 606−620

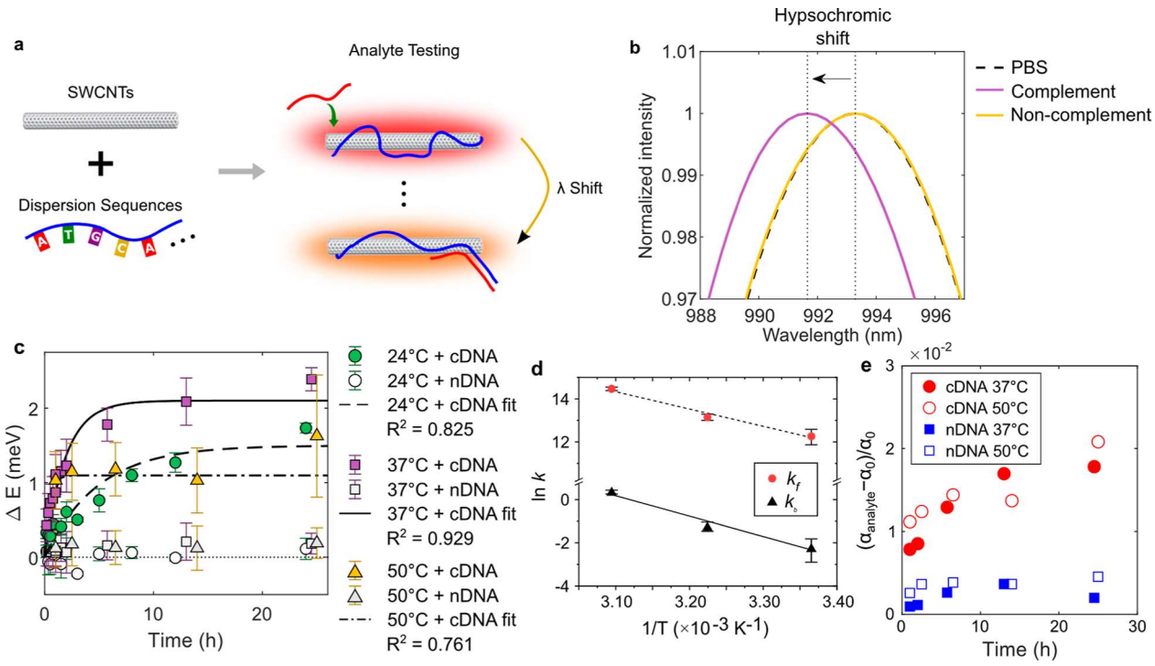

Figure 1. SWCNTs with the single-stranded DNA (ssDNA) corona for the detection of viral nucleic acid through hybridization. (a) Schematic of the ssDNA-functionalized SWCNT for detecting the target nucleic acid (analyte). Upon incubation, the target nucleic acid in solution hybridizes with the adsorbed ssDNA strands on the SWCNT surface, resulting in a measurable wavelength modulation of the SWCNT fluorescence signal. (b) An example of observed hypsochromic shifts in the PL spectra of the DNA-SWCNT construct near 990 nm upon incubation with the target complementary analyte. No shift was observed in noncomplementary control and PBS buffer. (c) Kinetics of the SWCNT 990 nm peak optical transition energy shift ($E_{Analyte} - E_0$) upon incubation with cDNA or nDNA at 24, 37, or 50 °C, fitted with the Langmuir adsorption model. $E_{Analyte}$ and E_0 denote the transition energy after and before analyte addition, respectively. Data presented as mean ± s.d., $n = 3$. (d) Arrhenius plots of the hybridization and denaturation rate constants obtained from the Langmuir adsorption model. The *R*-squared values for the fittings for k_f (dashed) and k_b (solid) are 0.979 and 0.976, respectively. (e) Normalized change in the DNA surface coverage of SWCNTs over time upon incubation with cDNA or nDNA at 37 or 50 °C. Specific adsorption occurs in the presence of cDNA but not nDNA.

reach the steady state for 24 and 37 °C, respectively, and only 2 h for 50 °C. This slower kinetics for hybridization on SWCNT CP compared to the hybridization of free DNA in the solution phase within minutes[65] indicates that there is polymer reorganization on the SWCNT surface. The response toward the complementary analyte at 37 °C showed a higher steady-state energy shift compared to 24 and 50 °C and less noise between triplicates compared to 50 °C. We attribute this difference in noise as a reduced thermodynamic stability of the hybridized complexes, which had a denaturing temperature of 56.2 °C.[66] This temperature-induced denaturation increases the distribution of SWCNTs between nonhybridized and hybridized states and experimental variability. Due to the latter point, studies were subsequently carried out at 37 °C for 1 h for data reliability.

To further characterize the hybridization kinetics, we used a Langmuir adsorption model assuming a reversible two-state hybridization without any intermediate

$$\text{cDNA (A)} + \text{adsorbed ssDNA (B)} \rightleftharpoons \text{hybridized duplex (AB)} \quad (1)$$

The rate constants of the forward and backward reactions are denoted by k_f and k_b, and the equilibrium constant is denoted by $K_{eq} \equiv k_f/k_b$. The rate of formation of the hybridized duplex can then be modeled using the following equation

$$\frac{dC_{AB}}{dt} = k_f C_A C_B - k_b C_{AB} \quad (2)$$

where C_A, C_B, and C_{AB} are the concentration of bulk cDNA in solution, the concentration of adsorbed ssDNA in the SWCNT CP that is available for hybridization, and the concentration of the hybridized duplex. All concentration units are normalized to the number of moles per volume. t is the time. According to the site balance, the total number of sites ($C_{B,0}$) can be calculated by summing the concentration of free sites (C_B) and the hybridized sites (C_{AB}). The rate of duplex formation can then be described by the following equation

$$\frac{dC_{AB}}{dt} = k_f C_A (C_{B,0} - C_{AB}) - k_b C_{AB} \quad (3)$$

The model further assumes that C_A is significantly higher than C_B such that C_A remains unchanged during the hybridization process. We assume that the SWCNT and its ssDNA corona have an approximate mass ratio of 1:1.[67] For a dispersion of 0.5 mg/L SWCNTs, the adsorbed ssDNA concentration is approximately 32 nM, much lower than the analyte concentration of 500 nM. Thus, the analytical solution of eq 2 with the initial condition of $C_{AB}(0) = 0$ is

$$C_{AB}(t) = \frac{C_A k_f}{k_b + C_A k_f} C_{B,0}(1 - e^{-(k_f C_A + k_b)t}) \quad (4)$$

https://doi.org/10.1021/acs.jpcc.2c06434
J. Phys. Chem. C 2023, 127, 606−620

The normalized concentration of the hybridized duplex can be correlated with the normalized energy shift $\frac{C_{AB}}{C_{AB,max}} = \frac{\Delta E}{\Delta E_{max}}$, where $C_{AB,max} = C_{B,0}$ is the maximum duplex concentration when hybridization reaches the steady state.[53] Solving for the fluorescence energy shift, we have eq 5 to fit to our dataset.

$$\Delta E(t) = \frac{C_A k_f}{k_b + C_A k_f} \Delta E_{max} (1 - e^{-(k_f C_A + k_b)t}) \quad (5)$$

The fitted models for 24, 37, and 50 °C are shown in Figure 1c, with k_f of $(2.18 \pm 0.75) \times 10^5$, $(5.16 \pm 0.75) \times 10^5$, and $(19.3 \pm 1.6) \times 10^5$ M^{-1} h^{-1}, respectively, and k_b of 0.109 ± 0.054, 0.293 ± 0.062, and 1.42 ± 0.12 h^{-1}, respectively. The hybridization rate constant k_f at 24 °C is similar to a previously reported value for a 22-mer DNA hybridization on SWCNTs at room temperature modeled using only the forward hybridization reaction.[53] According to the Arrhenius law, the rate constants of hybridization (the forward reaction) and denaturation (the backward reaction) are each associated with an activation energy, which are $E_{a,H}$ and $E_{a,D}$, respectively. By constructing an Arrhenius plot (Figure 1d), we found that $E_{a,H}$ is 66.7 kJ mol^{-1} and $E_{a,D}$ is 78.6 kJ mol^{-1}. Under the two-state hybridization assumption which is usually valid for short oligonucleotides,[68−70] the van't Hoff transition enthalpy of hybridization for this 22-mer DNA tested was calculated from $\Delta H_{vH} = -R\frac{d \ln K_{eq}}{dT^{-1}}$ to be −11.9 kJ mol^{-1}, which is more positive than that of a 21-mer DNA hybridizing with a perfect match in solution (−707 kJ mol^{-1})[65] and is rather on the scale of dimer duplex formation in solution (−44.4 to −30.1 kJ mol^{-1}).[71] This indicates that DNA hybridization on SWCNT CPs displays a smaller thermodynamic driving force compared to that in solution, likely due to conformational constraints on SWCNTs. Nevertheless, for a field-effect transistor system composed of 10-mer ssDNA covalently attached to SWCNT, the computed $E_{a,H}$ and $E_{a,D}$ were 142−202 and 225−398 kJ mol^{-1}, respectively.[29] This suggests that the covalently attached DNA has greater energy barriers to hybridization, likely due to constraints on the number of available conformations.

To estimate the SWCNT corona-phase surface coverage or solvent-exposed surface area, we computed the SWCNT surface effective dielectric constant through the measured solvatochromic shifts and ratiometrically compared the results to a reference. A semiempirical functional form of the SWCNT diameter solvatochromic shift was previously described.[51,72]

$$(E_{ii})^2 \Delta E_{ii} = -Lk\left[\frac{2(\varepsilon - 1)}{2\varepsilon + 1} - \frac{2(n^2 - 1)}{n^2 + 1}\right]\frac{1}{R^4} = \frac{C}{d^4} \quad (6)$$

where E_{ii} is the optical transition energy, $\Delta E_{ii} = E_{ii} - E_{11}^{Air}$ is the difference between the optical transition energy in the dielectric environment (E_{ii}) and the optical transition energy of the pristine SWCNT in air (E_{11}^{Air}), L is a fluctuation factor, k is a scaling constant of the SWCNT polarizability, ε is the static dielectric constant, n is the refractive index, R is the nanotube radius, and d is the nanotube diameter. The constant C gathers all the parameters that are constant for a specific chirality. In this work, the E_{11} optical transitions of the (6,5), (7,5), and (9,4) SWCNTs were calculated via background fitting of the PL spectra. The optical transitions in air were then calculated according to

$$E_{11}^{Air} = \frac{hc}{A_1 + A_2 d} + A_3 \frac{\cos\theta}{d^2} \quad (7)$$

where h is Planck's constant, c is the speed of light, d is the SWCNT diameter, θ is the chiral angle corresponding to the SWCNT chirality (n,m), A_1 = 61.1 nm, and A_2 = 1,113.6. By noting mod$((n - m), 3) = j$, $A_3 = -0.077$ eV nm^2 for $j = 1$ and $A_3 = 0.032$ eV nm^2 for $j = 2$.

The proportionality constant C from eq 6 was obtained by plotting $(E_{ii})^2 \Delta E_{ii}$ against $1/d^4$ for the different chiralities to calculate the slope from linear fitting. By comparing the constant to the slope of a reference system of the SWCNT suspended in *N*-methyl-2-pyrrolidone (NMP), the effective dielectric constant, ε_{eff}, can be calculated by

$$\frac{C}{C_{NMP}} = \frac{\frac{\varepsilon_{eff} - 1}{2\varepsilon_{eff} + 1} - \frac{n^2 - 1}{2n^2 + 1}}{\frac{\varepsilon_{NMP} - 1}{2\varepsilon_{NMP} + 1} - \frac{n_{NMP}^2 - 1}{2n_{NMP}^2 + 1}} \quad (8)$$

where C_{NMP} = 0.060 eV^3 nm,[4] ε_{NMP} = 32.2, n_{NMP} = 1.47, and n is the refractive index of DNA wrappings in water, which is equal to that of water (n = 1.333). Finally, we assume that the SWCNT surface coverage reflects a linear contribution from the solvent (water) and DNA wrappings to ε_{eff}. The relative surface coverage of the SWCNT by its DNA wrapping, α, can be estimated by

$$\varepsilon_{eff} = \alpha\varepsilon_{DNA} + (1 - \alpha)\varepsilon_{Water} \quad (9)$$

where ε_{DNA} is the dielectric constant of the DNA wrappings (ε_{DNA} = 4)[73] and ε_{Water} is the dielectric constant of water (ε_{Water} = 88.1). Calculation of the surface coverage in this way is convenient and sufficient for this work. An alternative called the molecular probe adsorption (MPA) method would be to use the adsorption of fluorescent molecular probes for each of the experimental conditions.[74] The correlation between the solvatochromic surface coverage and MPA will be the topic of a future study, but we do not expect the difference to substantially change the conclusions of this current work.

To compare the results between experimental conditions, we calculate $(\alpha_{Analyte} - \alpha_0)/\alpha_0$. The surface coverage upon PBS buffer addition, α_0, is considered as the initial DNA surface coverage without the introduction of the solution-phase analyte. A positive value means an increase in nanotube surface coverage by DNA, resulting in a denser surface packing and negative values and vice versa. As shown in Figure 1e, the SWCNT wrapping coverage increased upon complementary cDNA addition at both 37 and 50 °C, while nDNA had no effect. Thus, hybridization resulted in a denser packing of the SWCNT surface, while the nDNA was precluded.

Adsorbed Strand Sequence Dependence on Hybridization Outcomes. While adsorbed, DNA conformation on the SWCNT surface likely interferes with the traditional geometries of nucleotide hybridization. Hybridization may occur on the SWCNT surface, in solution following partial detachment, or both. Previous work showed that an optimal "anchor sequence" may exist to assist both the SWCNT dispersion and presentation of the complementary strand for hybridization (Figure 1a).[54] Anchor sequences, as the name suggests, were designed to adsorb to the SWCNT surface strongly such that the likelihood of complement regions desorbing to interact with solution-phase analytes increases. In this configuration, it was argued that the anchor length is

https://doi.org/10.1021/acs.jpcc.2c06434
J. Phys. Chem. C 2023, 127, 606−620

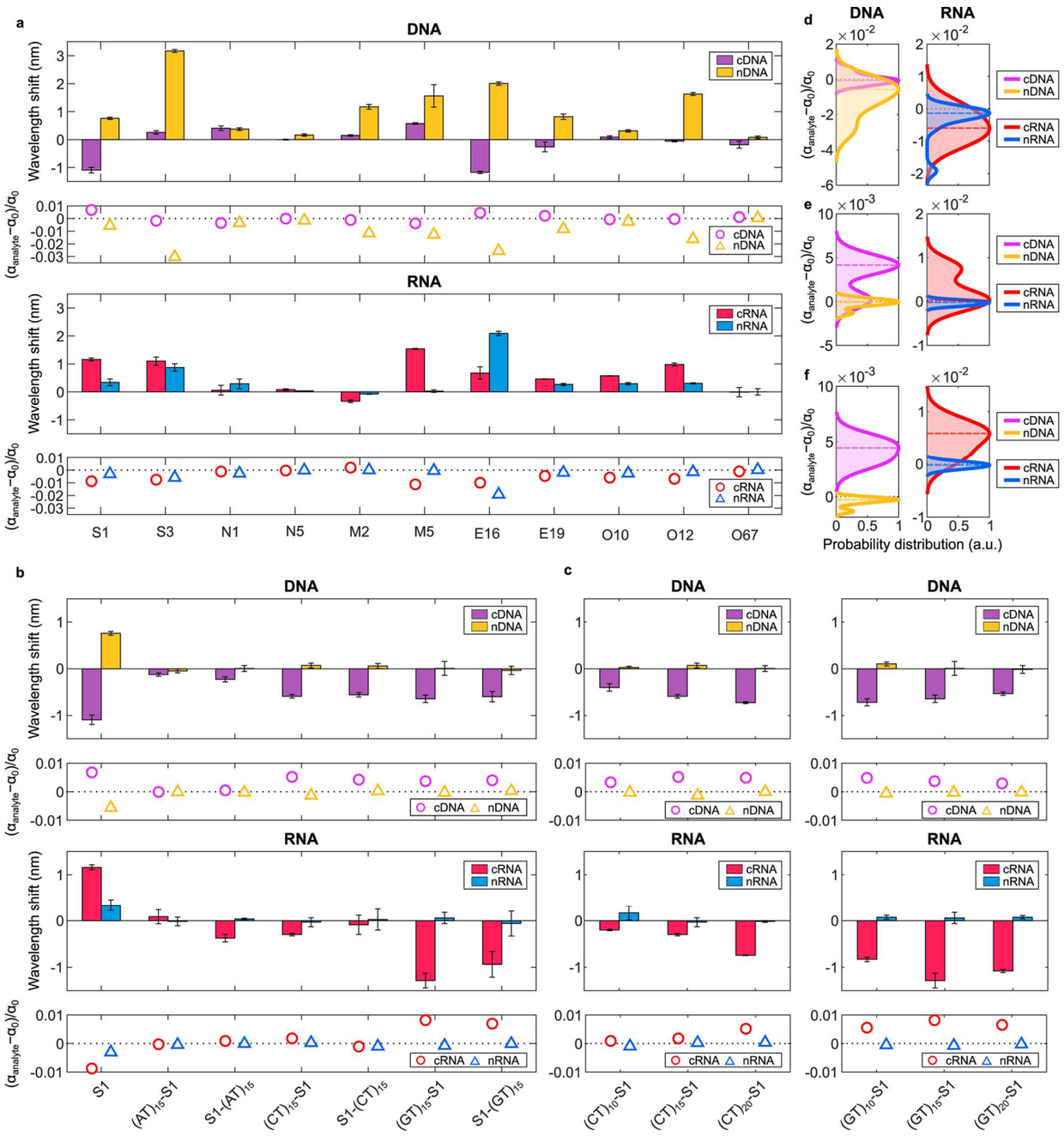

Figure 2. Influence of the anchor in the adsorbed strand on SWCNT wavelength modulation and surface coverage. (a) Responses of 11 ssDNA-SWCNT complexes toward 11 unique sequences from SARS-CoV-2 in Table 1. The ssDNA used to functionalize SWCNT contains only the complementary region without an anchor region. Both DNA (top panel) and RNA (bottom panel) complementary and noncomplementary analytes elicited mainly bathochromic shifts. (b) Responses of S1 ssDNA-SWCNT complexes with the $(AT)_{15}$, $(CT)_{15}$, or $(GT)_{15}$ anchor and without anchor toward DNA (top panel) and RNA (bottom panel) analytes. The anchor was added to either the 5′ or the 3′ end of the complementary region. SWCNT PL responses toward nDNA and nRNA were significantly suppressed for constructs with an anchor region. (c) Responses of S1 ssDNA-SWCNT complexes with $(CT)_x$ (left panel) or $(GT)_x$ (right panel) anchor of different lengths (x = 10, 15, 20) toward DNA (top panel) and RNA (bottom panel) analytes. All data presented as mean ± s.d., n = 3. (d) Probability distribution of normalized surface coverage changes of 11 SWCNT constructs without anchors in (a) upon DNA (left panel) and RNA (right panel) analyte introduction. (e) Probability distribution of normalized surface coverage change of S1 SWCNT constructs with anchors in (b) upon DNA (left panel) and RNA (right panel) analyte introduction. (f) Probability distribution of normalized surface coverage change of S1 SWCNT constructs with $(CT)_x$ and $(GT)_x$ anchors in (c) upon DNA (left panel) and RNA (right panel) analyte introduction.

https://doi.org/10.1021/acs.jpcc.2c06434
J. Phys. Chem. C 2023, 127, 606−620

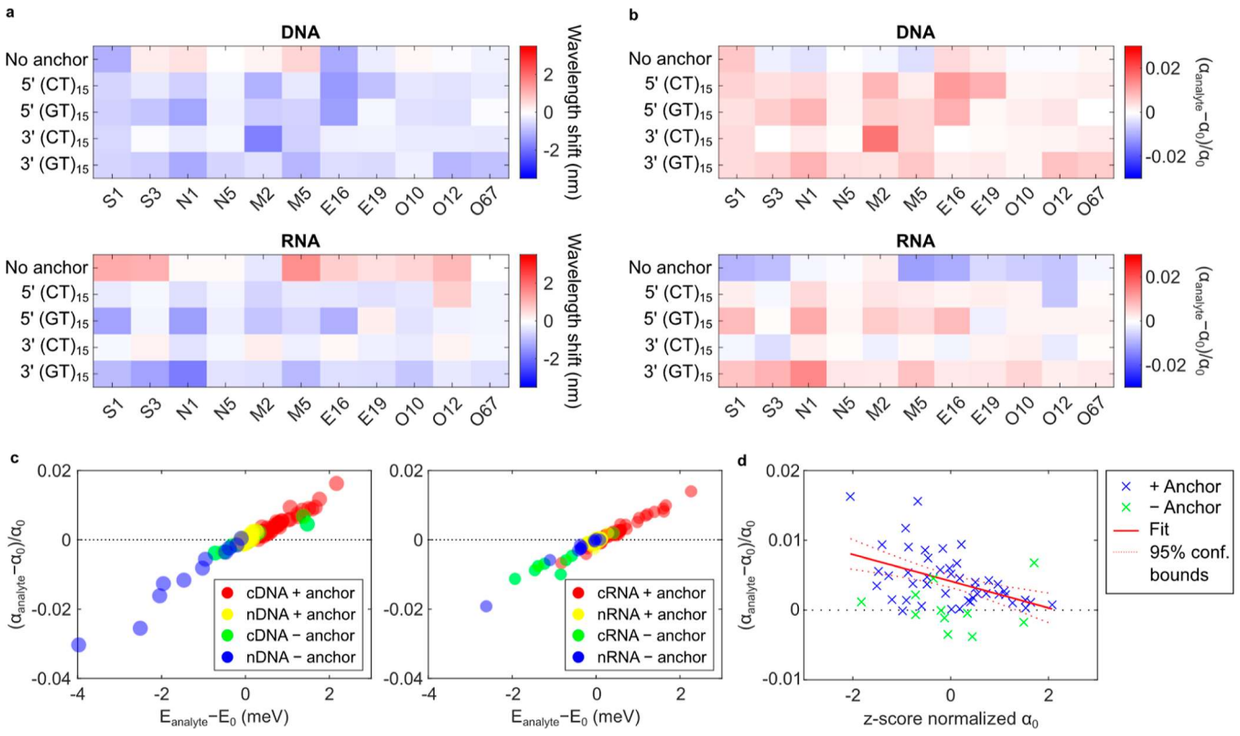

Figure 3. Screening results of the ssDNA-SWCNT library targeting 11 sequences. (a) Solvatochromic shifts and (b) normalized change in surface coverage by DNA upon incubation with 500 nM cDNA and cRNA. For each target sequence, four anchor regions were used, namely, $(CT)_{15}$ attached at the 5′ end, $(CT)_{15}$ attached at the 3′ end, $(GT)_{15}$ attached at the 5′ end, and $(GT)_{15}$ attached at the 3′ end of the complementary region. Red denotes a bathochromic shift in (a) and an increase in surface coverage in (b), while blue denotes a hypsochromic shift in (a) and a decrease in surface coverage in (b). The heat maps showing responses toward nDNA and nRNA controls are given in Figure S1. All data presented as mean, $n = 3$. (c) Scatter plots of normalized surface coverage change against optical transition energy change for CPs with and without anchors upon addition of DNA (left plot) and RNA analytes (right plot). (d) Correlations between normalized surface coverage change after cDNA addition and z-scored initial surface coverage before cDNA addition. A statistically significant negative correlation with a Pearson coefficient of −0.527 ($P < 0.001$) was observed for anchored CP denoted by the blue crosses. No meaningful correlation was observed for unanchored CPs denoted by the green crosses.

important to the accessibility of complement regions while being also not too far as to reduce solvatochromic effects.

To systematically understand the effects of the anchor segment, we created a test library of ssDNA-SWCNT comparing (1) the presence of the anchor, (2) the location of the anchor at the 5′ or 3′ end of the complementary region, (3) the length of the anchor, and finally (4) the anchor nucleotide composition (Tables S2 and S3).

As a control, we first tested SWCNT CPs without anchor segments. We found that the complementary analytes (cDNA and cRNA) gave inconsistent responses, while the non-complementary analytes (nDNA and nRNA) resulted in mostly bathochromic shifts and looser DNA surface coverage (Figure 2a). To better represent the results, we use the data set as a group to compare the probability distribution of the relative surface coverage changes following complement or random analyte addition (Figure 2d). These results graphically showed that the two distributions were unimodal and overlapping for both DNA and RNA.

To study the effect of introducing anchor segments, we used the S1 sequence as an example. We attached anchor segments of $(AT)_{15}$, $(CT)_{15}$, or $(GT)_{15}$ to either the 3′ or 5′ end of S1. The results from Figure 2b,e show that the inclusion of a 30-mer anchor imparted recognition specificity as shown by the hypsochromic shifts (increased surface coverage) in most experimental conditions, with the exception of $(AT)_{15}$ anchoring cRNA. We hypothesized that the anchor regions improve the surface adsorption of the CP, helping to specifically recruit complementary duplexes. According to the binding energy per nucleotide on SWCNTs determined by Iliafar et al.,[75] the 30-mer $(AT)_{15}$, $(CT)_{15}$, or $(GT)_{15}$ anchors correspond to an additional 921, 606, and 858 k_BT in binding energy, much greater than that of the S1 complementary region alone (594 k_BT). Comparing across the different anchor compositions, $(CT)_{15}$ and $(GT)_{15}$ exhibited a greater selective hypsochromic shift and greater surface coverage than $(AT)_{15}$ (Figure 2b). We attribute this difference to the likely self-hybridization effects of $(AT)_{15}$ between CP anchor regions, reducing the corona stability and presentation of the complementary region. Next, the 3′ or 5′ location of anchors did not show a significant difference (Figure 2b). Finally, we assessed the responses from sensors with anchors of different lengths (Figure 2c). We found that longer $(CT)_x$ anchor lengths (x = 10, 15, and 20) caused increased hybridization effects. While no such trend was found for the $(GT)_x$ anchors, its overall response was higher (Figure 2c). Given that guanine has a higher binding energy than cytosine on the SWCNT surface in the aqueous phase,[76−78] $(CT)_x$ anchors partially make up for the difference via length. Nonetheless, the inclusion of $(CT)_x$ and $(GT)_x$ anchors of any length led to

https://doi.org/10.1021/acs.jpcc.2c06434
J. Phys. Chem. C 2023, 127, 606−620

Table 2. *p*-Values of Paired, Two-Tailed Nonparametric Wilcoxon Signed Rank Tests with a Significance Level of 0.05 on the Impacts of Anchor Composition and Location on PL Responses

		DNA analytes		RNA analytes	
		solvatochromic shift	normalized surface coverage change	solvatochromic shift	normalized surface coverage change
$(CT)_{15}$ vs $(GT)_{15}$	5′	$P = 0.779$	$P = 0.765$	$P = 0.0186$	$P = 0.0244$
	3′	$P = 0.083$	$P = 0.102$	$P < 0.001$	$P < 0.001$
5′ vs 3′	$(CT)_{15}$	$P = 0.175$	$P = 0.24$	$P = 0.042$	$P = 0.083$
	$(GT)_{15}$	$P = 0.577$	$P = 0.52$	$P = 0.206$	$P = 0.206$

Table 3. Summary of Pearson's Correlation Coefficient (R) and *p*-Value (P) of Correlations between Analyte Properties and SWCNT Photophysical Property Changes

analyte property	analyte	CP anchor	solvatochromic shift	normalized surface coverage change	supplementary figure
N_{Dm}	cDNA	5′ $(GT)_{15}$	$R = 0.832$	$R = -0.822$	Figure S16b
			$P = 0.00148$	$P = 0.0019$	Figure S17b
N_{Dm}	cRNA	5′ $(GT)_{15}$	$R = 0.653$	$R = -0.678$	Figure S16g
			$P = 0.0294$	$P = 0.022$	Figure S17g
ΔG_{Hp}	cDNA	5′ $(CT)_{15}$	$R = -0.871$	$R = 0.733$	Figure S4a
			$P = 0.001$	$P = 0.016$	Figure S5a
L_{Min}	cRNA	3′ $(GT)_{15}$	$R = -0.703$	$R = 0.727$	Figure S14i
			$P = 0.0158$	$P = 0.0112$	Figure S15i
thymine content	cDNA	5′ $(CT)_{15}$	$R = -0.812$	$R = 0.783$	Figure S20a
			$P = 0.00238$	$P = 0.00437$	Figure S21a
cytosine content	cRNA	3′ $(GT)_{15}$	$R = -0.646$	$R = 0.65$	Figure S22i
			$P = 0.0317$	$P = 0.0303$	Figure S23i

hybridization specificity, as clearly shown by the distinctly shifted probability distributions in Figure 2f. Given these anchor study results, we designed a library of ssDNA-SWCNT containing $(CT)_{15}$ or $(GT)_{15}$ anchors to further study the responses of our system to the library of DNA and RNA analytes.

Screening Results against Target Sequences. A library of ssDNA was created to suspend SWCNTs to target each of the aforementioned analyte sequences. Each ssDNA was composed of $(CT)_{15}$ or $(GT)_{15}$ anchor adjacent to either the 5′ or 3′ end of the complementary segment. The results showed that most of the constructs with anchors showed significant hypsochromic shifts in PL spectra toward cDNA and cRNA compared to the bathochromic shifts without anchors (Figure 3a). Successful hybridization for constructs with anchors was further confirmed by the denser DNA wrapping on the nanotube surface upon cDNA and cRNA introduction as shown in Figure 3b. Negligible responses were shown for random controls (Figure S1a,b). In a scatter plot of PL emission energy shift versus surface coverage change, we showed that the larger and more predictable responses came from the presence of anchors and complement sequences (Figure 3c).

Looking at the data set as a whole, we found a linear correlation between the initial SWCNT surface coverage and its hybridization response (Figure 3d). The negative correlation indicates that a loosely packed CP could accommodate more complementary targets for hybridization. This was not seen in nonanchored results (Figure S2), suggesting that the anchor plays a major role in analyte recruitment.

We statistically investigated the impacts of anchor composition, $(CT)_{15}$ or $(GT)_{15}$, and location, 5′ or 3′, on PL responses, as shown in Table 2. For detecting RNA targets only, constructs with $(GT)_{15}$ anchor regardless of attachment location demonstrated greater hypsochromic shifts and a greater increase in surface coverage upon hybridization compared to those with the $(CT)_{15}$ anchor. This could be attributed to the stronger adsorption strength of the $(GT)_{15}$ anchor (858 k_BT) on the SWCNT surface than the $(CT)_{15}$ anchor (606 k_BT), leading to stronger adsorption stability for the hybridized duplex. The anchor location did not show a clear trend.

As a separate control, we tested prehybridized double-stranded DNA (dsDNA) as analytes on our best DNA-performing constructs (M2-$(CT)_{15}$, $(CT)_{15}$-E16) (Figure S3). All dsDNA experimental conditions, noncomplement or complement, produced negligible PL responses. This is consistent with our thermodynamic estimates that solution-phase canonical hybridization is favored over its SWCNT CP counterpart. As a result, we further hypothesized that secondary structure formation within analyte strands (e.g., hairpins and self-dimers), although designed to be minimal by prediction, would be unavoidable in reality and similarly contribute to attenuated PL responses.

To test the above hypothesis and study analyte sequence property dependence, we used the following metrics as features of the analyte sequences (Figures S4 and S25). We correlated these features to our sensor responses to gain an understanding of which features influence the hybridization events. Further description of each metric can be found in the Supporting Information.

(1) Most negative free energy of hairpin formation among all potential hairpins, ΔG_{Hp}
(2) % length of the shortest single-stranded section among all hairpins, L_{Hp}
(3) Free energy of hybridization, ΔG_{Hyb}
(4) Most negative free energy of self-dimerization among all potential self-dimers, ΔG_{Dm}
(5) % length of the single-stranded section of the self-dimer in (4), L_{Dm}
(6) Minimum of (2) and (5), L_{Min}

https://doi.org/10.1021/acs.jpcc.2c06434
J. Phys. Chem. C 2023, 127, 606−620

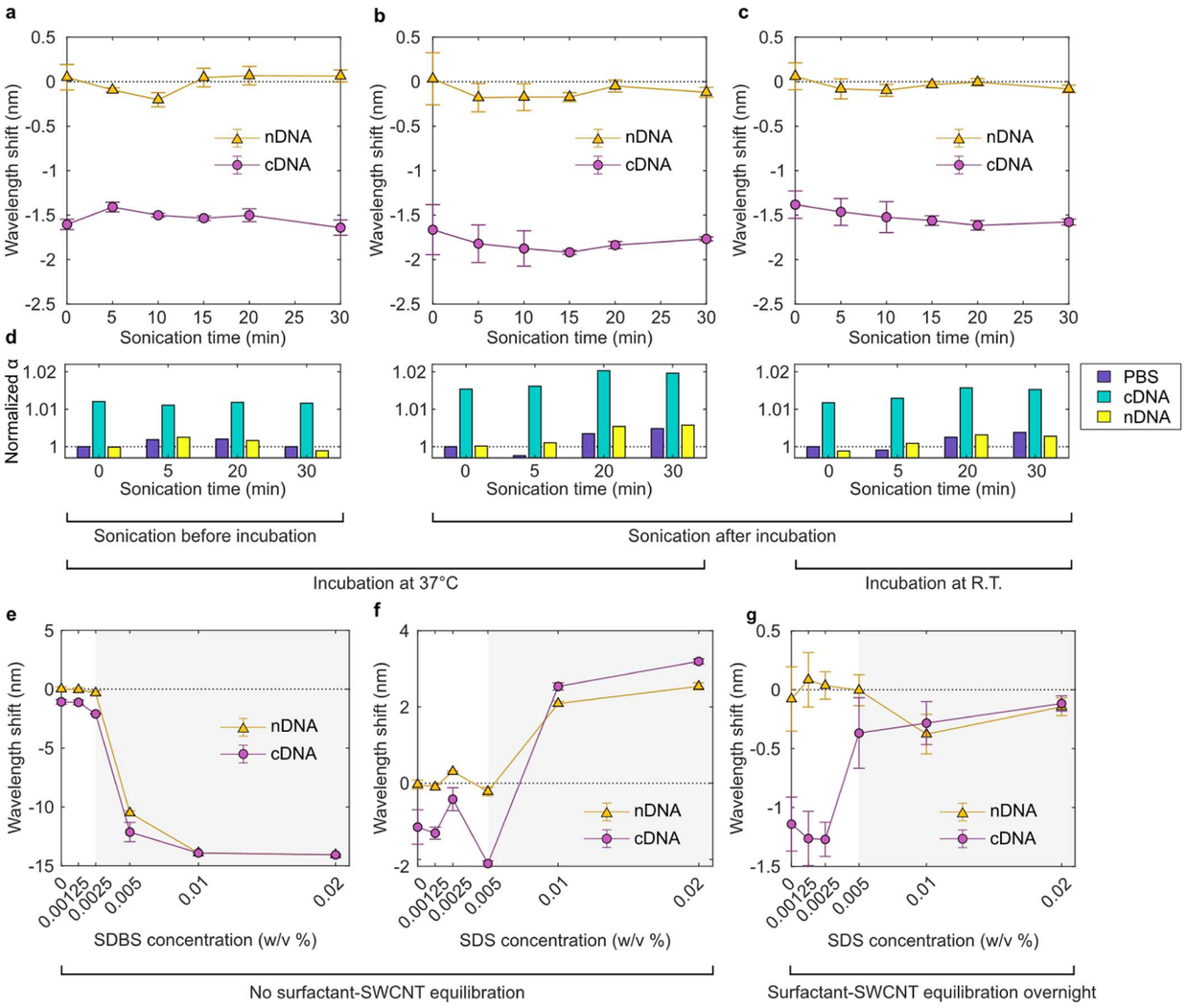

Figure 4. Influence of incubation conditions on sensor solvatochromic responses and surface coverage change. (a–c) M2-$(CT)_{15}$-SWCNT solvatochromic responses when bath sonication was carried out (a) after the 1 h incubation at 37 °C, (b) before the 1 h incubation at 37 °C, or (c) before the 1 h incubation at room temperature. Conditions are listed below (d). (d) Surface coverage of M2-$(CT)_{15}$-SWCNT in (a–c) normalized to the initial surface coverage without sonication (PBS addition, 0 min sonication). (e) Solvatochromic responses when SDBS was added to the dispersion concurrently with the analyte before incubation. (f) Response when SDS was added concurrently with the analyte before incubation. (g) Response when SDS was added to the SWCNT dispersion 12 h before the analyte was added. Amphiphilic molecules decreased the response specificity. Gray shaded regions represent surfactant concentration ranges beyond which response specificity started to worsen. Conditions are listed below. All data presented as mean ± s.d., n = 3.

(7) Number of unique self-dimers possible, N_{Dm}
(8) A, T, G, and C content individually

We calculated the correlation coefficients between these analyte properties and SWCNT PL responses, grouped by the anchor type (5′/3′ and $(CT)_{15}/(GT)_{15}$). Statistically significant correlations are shown in Table 3.

From the correlations in Table 3, the secondary structure within analyte strands negatively impacts its capability to hybridize with ssDNA-SWCNTs. The negative correlation between N_{Dm} and normalized surface coverage change indicates that increased self-dimer formation disfavors SWCNT surface adsorption. Similarly, hairpin formation disfavors SWCNT surface adsorption, as shown by the positive correlation between ΔG_{Hp} and the relative change of DNA surface coverage. Additionally, L_{Min} correlations suggested that the loss of single-stranded regions to secondary structures adversely impacts SWCNT surface hybridization.

Next, we looked into the effects of individual nucleotides on PL responses. Both T and C contents in the analyte sequences are positively correlated with PL responses. Previously, a single-nucleotide SWCNT binding study showed a preference ordering of A > G > T > C.[75] The analyte T/C content translates to a higher CP A/G content, which should more aggressively adsorb analyte strands to the SWCNT surface, leading to denser packing. Other analyte properties did not demonstrate statistically significant correlations (Figures S6–S13, S18, S19, S24, and S25).

Condition-Dependent Analyte Responses. The fact that both cDNA and cRNA generated selective responses demonstrated the versatility of our approach. The sequences

https://doi.org/10.1021/acs.jpcc.2c06434
J. Phys. Chem. C 2023, 127, 606–620

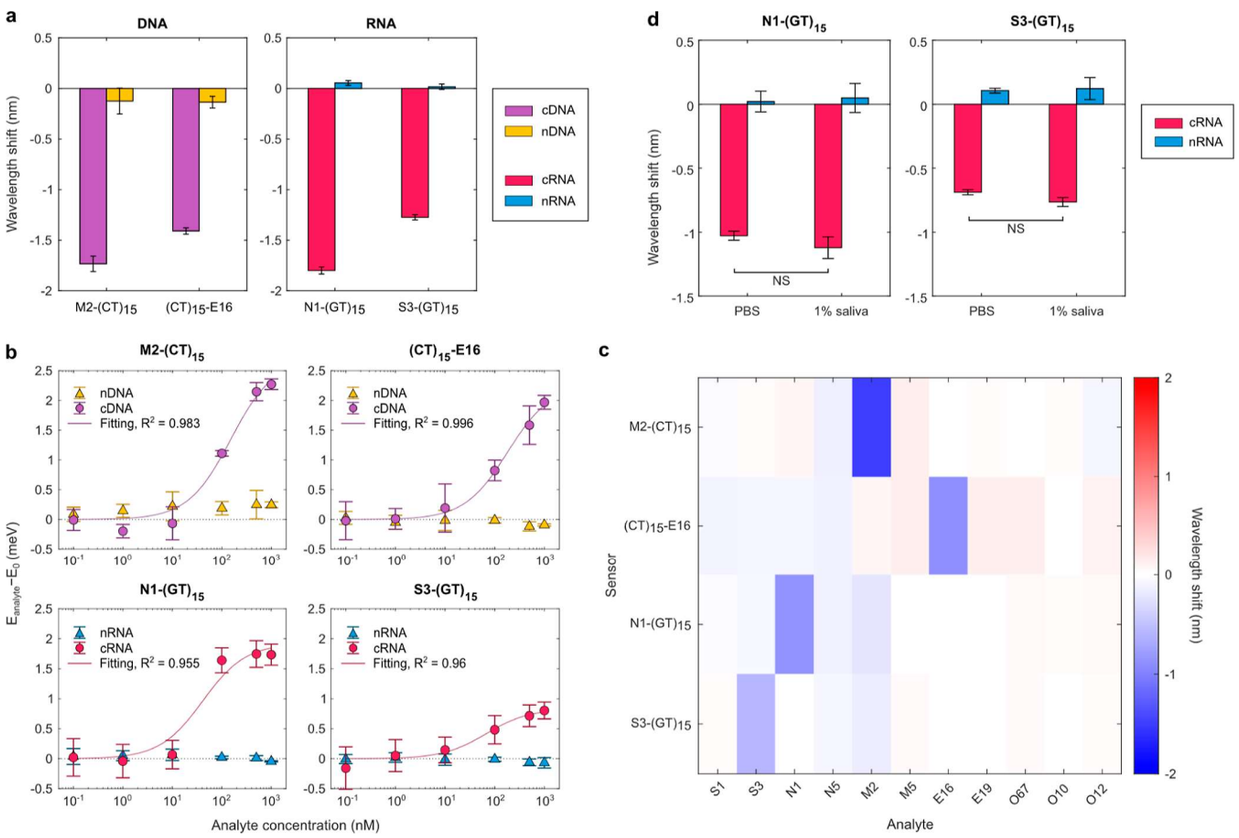

Figure 5. Summary of the best constructs for detecting complementary DNA and RNA targets, their detection limits, specificity, and responses in biofluids. (a) Responses of the best two DNA and best two RNA detecting constructs against 500 nM complementary and noncomplementary analytes. (b) Calibration curves showing energy shifts toward 0.1 to 1000 nM analytes fitted to the Langmuir binding model to quantify the kinetic parameters. Fitting parameters are α = 2.692 ± 0.7, 2.261 ± 0.285, 1.92 ± 0.54, and 0.833 ± 0.247 meV, and K_D = 150.8 ± 148, 181.3 ± 81.2, 41 ± 64.6, and 67.3 ± 97.6 nM for M2-$(CT)_{15}$, $(CT)_{15}$-E16, N1-$(GT)_{15}$, and S3-$(GT)_{15}$, respectively. (c) Heat map showing the responses toward 1 complementary target sequence and 10 noncomplementary sequences at 500 nM. Red: bathochromic shift, blue: hypsochromic shift. Responses demonstrate that complementary target-induced hypsochromic shift or an increase in energy is specific over noncomplementary sequences. (d) Responses of N1-$(GT)_{15}$ and S3-$(GT)_{15}$ toward 500 nM cRNA and nRNA in PBS buffer and 1% saliva. Solvatochromic shifts when the ssDNA-SWCNT construct was diluted in PBS buffer and 1% saliva do not show a significant difference using a two-sample *t*-test analysis (P = 0.127 for N1-$(GT)_{15}$ and P = 0.0573 for S3-$(GT)_{15}$). NS: not significant. All data presented as mean ± s.d., n = 3.

that had the largest PL responses are M2-$(CT)_{15}$ and $(CT)_{15}$-E16 for cDNA and N1-$(GT)_{15}$ and S3-$(GT)_{15}$ for cRNA. We chose these constructs to study their potential as photophysical sensors. Considering that hybridization events occur on the ssDNA-SWCNT CP, we explored two methods that potentially can affect CP rearrangement during binding events: (1) bath sonication and (2) the surfactant.

For the bath sonication treatment studies, we hypothesize that preanalyte ultrasonication could prime the CP, and postanalyte ultrasonication can improve the slow kinetics of the CP rearrangement. Ultrasonicator power, water levels, sample volume, and sample location within the bath were all kept constant to control for variability. M2-$(CT)_{15}$ was used to study ultrasonication effects. In general, bath sonication up to 30 min did not significantly alter PL responses in any configuration (Figure 4a–c). In corresponding surface coverage results, postincubation sonication for 20 or 30 min showed increased surface coverage for complementary analytes. Unfortunately, the surface coverage also increased for PBS and random controls. For the associated RNA experiments, we made similar observations (Figure S24a–d). Overall, this bath sonication approach would confound results when used for sensing purposes.

For the surfactant treatment studies, we followed up on previous work showing that sodium dodecylbenzene sulfonate (SDBS)[79] and sodium dodecyl sulfate (SDS)[80] addition improved PL responses. These amphiphilic molecules are commonly used to debundle SWCNTs by adsorbing to the SWCNT surface (benzene ring and long alkyl chain for SDBS and long alkyl chain for SDS) and interfacing with the aqueous solution via the small hydrophilic sulfonate head group. Addition of SDBS[31] and SDS[32] to ssDNA-SWCNT sensor dispersions previously enhanced the hybridization-induced wavelength modulation without losing sequence specificity. We used $(CT)_{15}$-E16-SWCNT to study these surfactant effects over a range of concentrations (0, 0.00125, 0.0025, 0.005, 0.01, and 0.02 w/v %) below the critical micelle concentrations. Two experimental conditions were tested, either with surfactant preincubation with ssDNA-SWCNT or coincubation during the 1 h analyte exposure.

SDBS coincubation at low concentrations (0.0025%) showed a 94% increase in hypsochromic shift (Figure 4e).

https://doi.org/10.1021/acs.jpcc.2c06434
J. Phys. Chem. C 2023, 127, 606−620

However, increasing SDBS concentrations further resulted in PL response from noncomplement analytes, eventually converging analyte responses to the same value. We attribute these results to SDBS replacing the adsorbed ssDNA on the SWCNT surface and leaving the SWCNT CP more densely packed in a nonselective manner. The SDS addition experiments did not show any PL response improvements in the conditions tested (Figure 4f,g).

The threshold surfactant concentrations where specific responses were retained were 0.0025% for SDBS and 0.005% for SDS, showing that SDBS has a greater affinity for the SWCNT surface as expected.[81] To summarize, in our experimental design, surfactant addition did not show significant improvement in transducing hybridization events and was not employed further due to confounding effects.

Detection Limit, Specificity, and Compatibility in Biofluids. We tested the sensor response over a range of analyte concentrations and constructed a dose−response curve to determine the detection limit. Again, the best two DNA ($(CT)_{15}$-SWCNT and $(CT)_{15}$-E16-SWCNT) and RNA (N1-$(GT)_{15}$-SWCNT and S3-$(GT)_{15}$-SWCNT) detecting constructs were chosen (Figure 5a). A range of analyte concentrations from 0.1 to 1000 nM were chosen. Signal saturation occurred at 100−1000 nM (Figure 5b). Noncomplementary random controls showed overall no significant response. The equilibrium constant $K \equiv k_f/k_b$ defined earlier was determined from the aforementioned Langmuir binding model for each construct.[82−84] By rearranging eq 5, the energy shift at each analyte concentration after incubation can be written as

$$\Delta E = \beta \frac{C_A K}{1 + C_A K} \tag{10}$$

where β is a constant that summarizes all the constant terms in $\Delta E_{max}(1 - e^{-(k_f C_A + k_b)t})$ and t is 1 h for all analyte concentrations. The data in Figure 5b were found to generate fits to eq 10 with R^2 = 0.983, 0.996, 0.955, and 0.96 for M2-$(CT)_{15}$, $(CT)_{15}$-E16, N1-$(GT)_{15}$, and S3-$(GT)_{15}$, respectively. The resulting kinetic parameters were a = 2.692, 2.262, 1.921, and 0.833 meV, and the dissociation constant $K_D \equiv 1/K$ = 150.7, 181.3, 41, and 67.3 nM, respectively (Figure 5b). The limit of detection (LOD) is calculated using the formula LOD = $S_{blank} + 3\sigma_{blank}$, where S_{blank} is the theoretical wavelength shift without the presence of an analyte and σ_{blank} is the standard deviation of the response toward the PBS buffer. The limits of detection assuming this binding model were 11, 56, 13, and 131 nM, respectively. In the context of viral RNA detection, the LODs were converted to 12.8 $\log_{10}$, 13.5 $\log_{10}$, 12.9 $\log_{10}$, and 13.9 $\log_{10}$ copies of the viral genome with the assumption that each analyte has a single copy in the virus genome.

The specificity of the constructs toward noncomplementary analytes was studied by comparing the responses of M2-$(CT)_{15}$, $(CT)_{15}$-E16, N1-$(GT)_{15}$, and S3-$(GT)_{15}$ toward the 10 other analyte sequences from Table 1 at 500 nM. Specificity appears to be retained (Figure 5c).

Lastly, we assessed the compatibility of the ssDNA-SWCNT construct with a complex biofluid as a connection to obvious medical applications. For the context of viral RNA detection from patient samples, saliva was chosen as the target media because an oral swab is not only easier to administer compared to the blood or urine test but also more sensitive than the commonly employed nasal swab for the diagnosis of asymptomatic and mild COVID-19 infection.[85] Saliva contains a variety of electrolytes, proteins, polypeptides, polynucleotides, and small organic substances that can perturb the SWCNT ssDNA CP and interfere with the solvatochromic response.[86] However, the electrolytes and carbohydrate-based matrix in saliva should have minimal adsorption onto typical nanoparticle surfaces.[87] Previous reports of SWCNT-phospholipid-based sensors for the SARS-CoV-2 protein showed compatibility with saliva.[88] We introduced the commercially available saliva sample from pooled human donors at a final concentration of 1% v/v to the N1-$(GT)_{15}$ and S3-$(GT)_{15}$ construct dispersions. The PL shift amplitudes toward the target analytes showed no significant change between the PBS buffer condition and 1% v/v saliva. The response specificity over random control was also preserved (Figure 5d), suggesting that the nanotube CP is agnostic to the adsorption of saliva components at this saliva concentration to enable successful transduction of hybridization events.

CONCLUSIONS

Functionalizing SWCNTs with ssDNA presents a versatile and intuitive approach for the detection of single-stranded DNA and RNA oligonucleotides through hybridization and modulation of the SWCNT fluorescence signal. In this work, we systematically studied nucleotide hybridization on SWCNT CPs using SARS-COV-2 sequences as model analyte targets. Using a model of SWCNT solvatochromism, we explained the observed PL changes as a modulation in the SWCNT surface ssDNA coverage following complementary analyte addition. We find that hybridization on the SWCNT surface has a lower enthalpy (−11.9 kJ mol^{-1}) than in the solution phase (−707 kJ mol^{-1}). We also validated a previous approach by attaching an anchor region to the recognition region, which significantly improved PL response and selectivity, with $(GT)_{15}$ anchors superior to others tested. By correlating analyte sequence features to PL responses, we found that secondary structures such as hairpins and self-dimers are barriers to hybridization, suggesting that target sequence design is important for the overall detection process. We also varied incubation conditions to improve PL responses, bath sonication, and surfactant additions. Both showed ineffective improvements. Finally, the best ssDNA CP candidates demonstrate biocompatibility in complex media. The results of this study significantly improve the understanding of nanotube ssDNA CP interactions with solution-phase oligonucleotides.

The current study focuses on optimizing the sensor performance in vitro by investigating optimal sensor design and operating conditions. For the application of the sensor to detect viral genomes in patient samples, future work should be directed at improving the detection limit. The LODs of the best DNA and RNA detection constructs, when used in the solution phase as demonstrated in this study, in this work need to be improved by 7 orders of magnitude to detect the SARS-CoV-2 viral genome in patient saliva samples (5.2 $\log_{10}$ copies per mL).[89] When immobilized and probed at the single particle level, SWCNT sensors have been shown to resolve down to single-molecule detection limits.[72] Hence, a hardware design that allows massively parallel monitoring of single SWCNT fluorescent sensors should address this concern. As another strategy to improve the detection limit, an RNA amplification technique could be implemented prior to the sensor assay. Loop-mediated isothermal amplification (LAMP) is an excellent candidate due to its speed and simplicity. It

https://doi.org/10.1021/acs.jpcc.2c06434
J. Phys. Chem. C 2023, 127, 606−620

requires minimal sample purification from the crude sample, takes place under isothermal conditions, eliminating the need for expensive thermal cyclers, and, most importantly, creates products with long single-stranded loops of up to 100 mers which can function as the target sites.[90] As the dsDNA experiments have shown that the ssDNA-SWCNT is only compatible with single-strand oligonucleotides, the LAMP assay should be designed such that the single-stranded loops contain the target region for recognition. We demonstrate that this technique is agnostic to proteins and nucleotides present in biofluids and potentially remains so to LAMP assay enzymes. The versatility of this method and our findings pave the way for the rational design of ssDNA-SWCNT sensors against nucleotide targets, with potential implications for infectious disease management.

■ ASSOCIATED CONTENT

Supporting Information

The Supporting Information is available free of charge at https://pubs.acs.org/doi/10.1021/acs.jpcc.2c06434.

Description of target analyte metrics used in correlations; PL responses of ssDNA-SWCNT library against the random sequence analyte; PL responses after random sequence DNA analyte addition against initial surface coverage; PL responses to the dsDNA analyte; PL responses against target analyte metrics; PL responses to the RNA analyte with sonication and surfactant addition during incubation; and adsorbed strand and analyte sequences (PDF)

■ AUTHOR INFORMATION

Corresponding Author

Michael S. Strano − *Department of Chemical Engineering, Massachusetts Institute of Technology, Cambridge, Massachusetts 02139, United States;* orcid.org/0000-0003-2944-808X; Email: strano@mit.edu

Authors

Jianqiao Cui − *Department of Chemical Engineering, Massachusetts Institute of Technology, Cambridge, Massachusetts 02139, United States*

Xun Gong − *Department of Chemical Engineering, Massachusetts Institute of Technology, Cambridge, Massachusetts 02139, United States;* orcid.org/0000-0003-4168-2768

Soo-Yeon Cho − *School of Chemical Engineering, Sungkyunkwan University, Suwon 16419, Republic of Korea;* orcid.org/0000-0001-6294-1154

Xiaojia Jin − *Department of Chemical Engineering, Massachusetts Institute of Technology, Cambridge, Massachusetts 02139, United States*

Sungyun Yang − *Department of Chemical Engineering, Massachusetts Institute of Technology, Cambridge, Massachusetts 02139, United States*

Roya Khosravi-Far − *InnoTech Precision Medicine, Boston, Massachusetts 02130, United States*

Complete contact information is available at: https://pubs.acs.org/10.1021/acs.jpcc.2c06434

Author Contributions

#J.C. and X.G. contributed equally to the technical portion of this work. J.C., X.G., and M.S.S. conceived the project and devised the study. J.C. and X.G. synthesized the dispersions, performed the experiments, and analyzed the data. S.-Y.C., X.J., and S.Y. assisted with data analysis. R.K.-F. designed the target sequences. The manuscript was written using contributions from all of the listed authors. All authors have given approval for the final version of the manuscript.

Notes

The authors declare no competing financial interest.

■ ACKNOWLEDGMENTS

The authors are grateful for financial support from the NIH Radx Program and helpful discussions with R.K-F.. Financial support for this work was from the National Institutes of Health (NIH) Rapid Acceleration of Diagnostics (RADX) 1R42DE030829 to R.K-F., supporting sensor calibration and characterization measurements. The CP characterization efforts were partially supported by the NSF Biosensing Program, under award number 2124194 to M.S.S. Some of the data analysis effort was supported as part of the Disruptive & Sustainable Technology for Agricultural Precision (DiSTAP) of the Singapore MIT Alliance for Research and Technology (SMART) Center.

■ REFERENCES

(1) Tenover, F. C. DNA Hybridization Techniques and Their Application to the Diagnosis of Infectious Diseases. *Infect. Dis. Clin.* **1993**, *7*, 171−181.

(2) Sklar, J. DNA Hybridization in Diagnostic Pathology. *Hum. Pathol.* **1985**, *16*, 654−658.

(3) Chen, L.; Zhang, J.; Lin, Z.; Zhang, Z.; Mao, M.; Wu, J.; Li, Q.; Zhang, Y.; Fan, C. Pharmaceutical Applications of Framework Nucleic Acids. *Acta Pharm. Sin. B* **2022**, *12*, 76−91.

(4) Usher, P. A.; Galsgaard, E. D.; Kruse, K.; Wang, J.; Krogh, B. O.; Mandelbaum, J.; Almholt, K.Sensitive and Specific In Situ Hybridization for Early Drug Discovery BT - In Situ Hybridization Protocols. *In Situ Hybridization Protocols*; Nielsen, B. S., Ed.; Springer New York: New York, NY, 2014; pp 103−123.

(5) Rich, A. A Hybrid Helix Containing Both Deoxyribose and Ribose Polynucleotides and Its Relation to the Transfer of Information between the Nucleic Acids. *Proc. Natl. Acad. Sci. U.S.A.* **1960**, *46*, 1044−1053.

(6) Drmanac, R.; Drmanac, S.; Strezoska, Z.; Paunesku, T.; Labat, I.; Zeremski, M.; Snoddy, J.; Funkhouser, W. K.; Koop, B.; et al. DNA Sequence Determination by Hybridization: A Strategy for Efficient Large-Scale Sequencing. *Science* **1993**, *260*, 1649−1652.

(7) Vikrant, K.; Bhardwaj, N.; Bhardwaj, S. K.; Kim, K.-H.; Deep, A. Nanomaterials as Efficient Platforms for Sensing DNA. *Biomaterials* **2019**, *214*, 119215.

(8) Jayaraman, A.; Hall, C. K.; Genzer, J. Computer Simulation Study of Probe-Target Hybridization in Model DNA Microarrays: Effect of Probe Surface Density and Target Concentration. *J. Chem. Phys.* **2007**, *127*, 144912.

(9) Tymoczko, J.; Schuhmann, W.; Gebala, M. Electrical Potential-Assisted DNA Hybridization. How to Mitigate Electrostatics for Surface DNA Hybridization. *ACS Appl. Mater. Interfaces* **2014**, *6*, 21851−21858.

(10) Peterson, A. W.; Heaton, R. J.; Georgiadis, R. M. The Effect of Surface Probe Density on DNA Hybridization. *Nucleic Acids Res.* **2001**, *29*, 5163−5168.

(11) Shchepinov, M. S.; Case-Green, S. C.; Southern, E. M. Steric Factors Influencing Hybridisation of Nucleic Acids to Oligonucleotide Arrays. *Nucleic Acids Res.* **1997**, *25*, 1155−1161.

(12) Watterson, J. H.; Piunno, P. A. E.; Wust, C. C.; Krull, U. J. Effects of Oligonucleotide Immobilization Density on Selectivity of Quantitative Transduction of Hybridization of Immobilized DNA. *Langmuir* **2000**, *16*, 4984−4992.

(13) Vainrub, A.; Montgomery Pettitt, B. Surface Electrostatic Effects in Oligonucleotide Microarrays: Control and Optimization of Binding Thermodynamics. *Biopolymers* **2003**, *68*, 265−270.
(14) Traeger, J. C.; Schwartz, D. K. Surface-Mediated DNA Hybridization: Effects of DNA Conformation, Surface Chemistry, and Electrostatics. *Langmuir* **2017**, *33*, 12651−12659.
(15) Wong, I. Y.; Melosh, N. A. An Electrostatic Model for DNA Surface Hybridization. *Biophys. J.* **2010**, *98*, 2954−2963.
(16) Glazer, M. I.; Fidanza, J. A.; McGall, G. H.; Trulson, M. O.; Forman, J. E.; Frank, C. W. Kinetics of Oligonucleotide Hybridization to DNA Probe Arrays on High-Capacity Porous Silica Substrates. *Biophys. J.* **2007**, *93*, 1661−1676.
(17) Tawa, K.; Knoll, W. Mismatching Base-pair Dependence of the Kinetics of DNA−DNA Hybridization Studied by Surface Plasmon Fluorescence Spectroscopy. *Nucleic Acids Res.* **2004**, *32*, 2372−2377.
(18) Hooyberghs, J.; Van Hummelen, P.; Carlon, E. The Effects of Mismatches on Hybridization in DNA Microarrays: Determination of Nearest Neighbor Parameters. *Nucleic Acids Res.* **2009**, *37*, No. e53.
(19) Letowski, J.; Brousseau, R.; Masson, L. Designing Better Probes: Effect of Probe Size, Mismatch Position and Number on Hybridization in DNA Oligonucleotide Microarrays. *J. Microbiol. Methods* **2004**, *57*, 269−278.
(20) Stillman, B. A.; Tonkinson, J. L. Expression Microarray Hybridization Kinetics Depend on Length of the Immobilized DNA but Are Independent of Immobilization Substrate. *Anal. Biochem.* **2001**, *295*, 149−157.
(21) Halperin, A.; Buhot, A.; Zhulina, E. B. Brush Effects on DNA Chips: Thermodynamics, Kinetics, and Design Guidelines. *Biophys. J.* **2005**, *89*, 796−811.
(22) Sedighi, A.; Li, P. C. H.; Pekcevik, I. C.; Gates, B. D. A Proposed Mechanism of the Influence of Gold Nanoparticles on DNA Hybridization. *ACS Nano* **2014**, *8*, 6765−6777.
(23) Schneider, T.; Jahr, N.; Jatschka, J.; Csaki, A.; Stranik, O.; Fritzsche, W. Localized Surface Plasmon Resonance (LSPR) Study of DNA Hybridization at Single Nanoparticle Transducers. *J. Nanopart. Res.* **2013**, *15*, 1531.
(24) Dugas, V.; Depret, G.; Chevalier, Y.; Nesme, X.; Souteyrand, É. Immobilization of Single-Stranded DNA Fragments to Solid Surfaces and Their Repeatable Specific Hybridization: Covalent Binding or Adsorption? *Sens. Actuators, B* **2004**, *101*, 112−121.
(25) Wang, J.; Wang, L.; Liu, X.; Liang, Z.; Song, S.; Li, W.; Li, G.; Fan, C. A Gold Nanoparticle-based Aptamer Target Binding Readout for ATP Assay. *Adv. Mater.* **2007**, *19*, 3943−3946.
(26) Liu, B.; Liu, J. Interface-Driven Hybrid Materials Based on DNA-Functionalized Gold Nanoparticles. *Matter* **2019**, *1*, 825−847.
(27) Elghanian, R.; Storhoff, J. J.; Mucic, R. C.; Letsinger, R. L.; Mirkin, C. A. Selective Colorimetric Detection of Polynucleotides Based on the Distance-Dependent Optical Properties of Gold Nanoparticles. *Science* **1997**, *277*, 1078−1081.
(28) Li, H.; Rothberg, L. Colorimetric Detection of DNA Sequences Based on Electrostatic Interactions with Unmodified Gold Nanoparticles. *Proc. Natl. Acad. Sci. U.S.A.* **2004**, *101*, 14036−14039.
(29) Sorgenfrei, S.; Chiu, C.; Gonzalez, R. L.; Yu, Y.-J.; Kim, P.; Nuckolls, C.; Shepard, K. L. Label-Free Single-Molecule Detection of DNA-Hybridization Kinetics with a Carbon Nanotube Field-Effect Transistor. *Nat. Nanotechnol.* **2011**, *6*, 126−132.
(30) Barnes, B.; Wang, P.; Wang, Y. Parallel Field-Effect Nanosensors Detect Trace Biomarkers Rapidly at Physiological High-Ionic-Strength Conditions. *ACS Sens.* **2022**, *7*, 2537−2544.
(31) Harvey, J. D.; Jena, P. V.; Baker, H. A.; Zerze, G. H.; Williams, R. M.; Galassi, T. V.; Roxbury, D.; Mittal, J.; Heller, D. A. A Carbon Nanotube Reporter of MicroRNA Hybridization Events in Vivo. *Nat. Biomed. Eng.* **2017**, *1*, 41.
(32) Harvey, J. D.; Baker, H. A.; Ortiz, M. V.; Kentsis, A.; Heller, D. A. HIV Detection via a Carbon Nanotube RNA Sensor. *ACS Sens.* **2019**, *4*, 1236−1244.
(33) Loo, A. H.; Sofer, Z.; Bouša, D.; Ulbrich, P.; Bonanni, A.; Pumera, M. Carboxylic Carbon Quantum Dots as a Fluorescent Sensing Platform for DNA Detection. *ACS Appl. Mater. Interfaces* **2016**, *8*, 1951−1957.
(34) Qian, Z. S.; Shan, X. Y.; Chai, L. J.; Ma, J. J.; Chen, J. R.; Feng, H. A Universal Fluorescence Sensing Strategy Based on Biocompatible Graphene Quantum Dots and Graphene Oxide for the Detection of DNA. *Nanoscale* **2014**, *6*, 5671−5674.
(35) Ye, Y.-D.; Xia, L.; Xu, D.-D.; Xing, X.-J.; Pang, D.-W.; Tang, H.-W. DNA-Stabilized Silver Nanoclusters and Carbon Nanoparticles Oxide: A Sensitive Platform for Label-Free Fluorescence Turn-on Detection of HIV-DNA Sequences. *Biosens. Bioelectron.* **2016**, *85*, 837−843.
(36) Godavarthi, S.; Mohan Kumar, K. M.; Vázquez Vélez, E. V.; Hernandez-Eligio, A.; Mahendhiran, M.; Hernandez-Como, N.; Aleman, M.; Martinez Gomez, L. M. Nitrogen Doped Carbon Dots Derived from Sargassum Fluitans as Fluorophore for DNA Detection. *J. Photochem. Photobiol., B* **2017**, *172*, 36−41.
(37) Qiu, W.; Xu, H.; Takalkar, S.; Gurung, A. S.; Liu, B.; Zheng, Y.; Guo, Z.; Baloda, M.; Baryeh, K.; et al. Carbon Nanotube-Based Lateral Flow Biosensor for Sensitive and Rapid Detection of DNA Sequence. *Biosens. Bioelectron.* **2015**, *64*, 367−372.
(38) Lee, M. A.; Wang, S.; Jin, X.; Bakh, N. A.; Nguyen, F. T.; Dong, J.; Silmore, K. S.; Gong, X.; Pham, C.; et al. Implantable Nanosensors for Human Steroid Hormone Sensing In Vivo Using a Self-Templating Corona Phase Molecular Recognition. *Adv. Healthcare Mater.* **2020**, *9*, 2000429.
(39) Kruss, S.; Hilmer, A. J.; Zhang, J.; Reuel, N. F.; Mu, B.; Strano, M. S. Carbon Nanotubes as Optical Biomedical Sensors. *Adv. Drug Delivery Rev.* **2013**, *65*, 1933−1950.
(40) O'Connell, M. J.; Bachilo, S. M.; Huffman, C. B.; Moore, V. C.; Strano, M. S.; Haroz, E. H.; Rialon, K. L.; Boul, P. J.; Noon, W. H.; et al. Band Gap Fluorescence from Individual Single-Walled Carbon Nanotubes. *Science* **2002**, *297*, 593−596.
(41) Bachilo, S. M.; Strano, M. S.; Kittrell, C.; Hauge, R. H.; Smalley, R. E.; Weisman, R. B. Structure-Assigned Optical Spectra of Single-Walled Carbon Nanotubes. *Science* **2002**, *298*, 2361−2366.
(42) Wray, S.; Cope, M.; Delpy, D. T.; Wyatt, J. S.; Reynolds, E. O. R. Characterization of the near Infrared Absorption Spectra of Cytochrome Aa3 and Haemoglobin for the Non-Invasive Monitoring of Cerebral Oxygenation. *Biochim. Biophys. Acta, Bioenerg.* **1988**, *933*, 184−192.
(43) Cheong, W. F.; Prahl, S. A.; Welch, A. J. A Review of the Optical Properties of Biological Tissues. *IEEE J. Quantum Electron.* **1990**, *26*, 2166−2185.
(44) Weissleder, R.; Ntziachristos, V. Shedding Light onto Live Molecular Targets. *Nat. Med.* **2003**, *9*, 123−128.
(45) Wang, F.; Dukovic, G.; Brus, L. E.; Heinz, T. F. The Optical Resonances in Carbon Nanotubes Arise from Excitons. *Science* **2005**, *308*, 838−841.
(46) Heller, D. A.; Baik, S.; Eurell, T. E.; Strano, M. S. Single-Walled Carbon Nanotube Spectroscopy in Live Cells: Towards Long-Term Labels and Optical Sensors. *Adv. Mater.* **2005**, *17*, 2793−2799.
(47) Lew, T. T. S.; Park, M.; Cui, J.; Strano, M. S. Plant Nanobionic Sensors for Arsenic Detection. *Adv. Mater.* **2021**, *33*, 2005683.
(48) Zhang, J.; Landry, M. P.; Barone, P. W.; Kim, J.-H.; Lin, S.; Ulissi, Z. W.; Lin, D.; Mu, B.; Boghossian, A. A.; et al. Molecular Recognition Using Corona Phase Complexes Made of Synthetic Polymers Adsorbed on Carbon Nanotubes. *Nat. Nanotechnol.* **2013**, *8*, 959−968.
(49) Cognet, L.; Tsyboulski, D. A.; Rocha, J.-D. R.; Doyle, C. D.; Tour, J. M.; Weisman, R. B. Stepwise Quenching of Exciton Fluorescence in Carbon Nanotubes by Single-Molecule Reactions. *Science* **2007**, *316*, 1465−1468.
(50) Jin, H.; Heller, D. A.; Kalbacova, M.; Kim, J.-H.; Zhang, J.; Boghossian, A. A.; Maheshri, N.; Strano, M. S. Detection of Single-Molecule H2O2 Signalling from Epidermal Growth Factor Receptor Using Fluorescent Single-Walled Carbon Nanotubes. *Nat. Nanotechnol.* **2010**, *5*, 302−309.
(51) Choi, J. H.; Strano, M. S. Solvatochromism in Single-Walled Carbon Nanotubes. *Appl. Phys. Lett.* **2007**, *90*, 223114.

https://doi.org/10.1021/acs.jpcc.2c06434
J. Phys. Chem. C 2023, 127, 606−620

(52) Kruss, S.; Landry, M. P.; Vander Ende, E.; Lima, B. M. A.; Reuel, N. F.; Zhang, J.; Nelson, J.; Mu, B.; Hilmer, A.; et al. Neurotransmitter Detection Using Corona Phase Molecular Recognition on Fluorescent Single-Walled Carbon Nanotube Sensors. *J. Am. Chem. Soc.* **2014**, *136*, 713−724.
(53) Jeng, E. S.; Moll, A. E.; Roy, A. C.; Gastala, J. B.; Strano, M. S. Detection of DNA Hybridization Using the Near-Infrared Band-Gap Fluorescence of Single-Walled Carbon Nanotubes. *Nano Lett.* **2006**, *6*, 371−375.
(54) Jeong, S.; González-Grandío, E.; Navarro, N.; Pinals, R. L.; Ledesma, F.; Yang, D.; Landry, M. P. Extraction of Viral Nucleic Acids with Carbon Nanotubes Increases SARS-CoV-2 Quantitative Reverse Transcription Polymerase Chain Reaction Detection Sensitivity. *ACS Nano* **2021**, *15*, 10309−10317.
(55) Wu, S.-J.; Schuergers, N.; Lin, K.-H.; Gillen, A. J.; Corminboeuf, C.; Boghossian, A. A. Restriction Enzyme Analysis of Double-Stranded DNA on Pristine Single-Walled Carbon Nanotubes. *ACS Appl. Mater. Interfaces* **2018**, *10*, 37386−37395.
(56) Toyofuku, R.; Ohura, S.; Ito, M.; Homma, Y.; Umemura, K. Interactions of Secondary DNA and Initial DNA on Single-Walled Carbon Nanotube Surfaces Studied by Photoluminescence, Atomic Force Microscopy, and Electrophoresis. *J. Nanomater.* **2019**, *2019*, 2875439.
(57) Markham, N. R.; Zuker, M.UNAFold. *Bioinformatics: Structure, Function and Applications*; Keith, J. M., Ed.; Humana Press: Totowa, NJ, 2008; pp 3−31.
(58) Nakashima, N.; Okuzono, S.; Murakami, H.; Nakai, T.; Yoshikawa, K. DNA Dissolves Single-Walled Carbon Nanotubes in Water. *Chem. Lett.* **2003**, *32*, 456−457.
(59) Zheng, M.; Jagota, A.; Semke, E. D.; Diner, B. A.; Mclean, R. S.; Lustig, S. R.; Richardson, R. E.; Tassi, N. G. DNA-Assisted Dispersion and Separation of Carbon Nanotubes. *Nat. Mater.* **2003**, *2*, 338−342.
(60) Salem, D. P.; Gong, X.; Liu, A. T.; Koman, V. B.; Dong, J.; Strano, M. S. Ionic Strength-Mediated Phase Transitions of Surface-Adsorbed DNA on Single-Walled Carbon Nanotubes. *J. Am. Chem. Soc.* **2017**, *139*, 16791−16802.
(61) Zhang, J.; Kruss, S.; Hilmer, A. J.; Shimizu, S.; Schmois, Z.; De La Cruz, F.; Barone, P. W.; Reuel, N. F.; Heller, D. A.; et al. A Rapid, Direct, Quantitative, and Label-Free Detector of Cardiac Biomarker Troponin T Using Near-Infrared Fluorescent Single-Walled Carbon Nanotube Sensors. *Adv. Healthcare Mater.* **2014**, *3*, 412−423.
(62) Gan, H. H.; Pasquali, S.; Schlick, T. Exploring the Repertoire of RNA Secondary Motifs Using Graph Theory; Implications for RNA Design. *Nucleic Acids Res.* **2003**, *31*, 2926−2943.
(63) Wan, Y.; Kertesz, M.; Spitale, R. C.; Segal, E.; Chang, H. Y. Understanding the Transcriptome through RNA Structure. *Nat. Rev. Genet.* **2011**, *12*, 641−655.
(64) Gong, X.; Renegar, N.; Levi, R.; Strano, M. S. Machine Learning for the Discovery of Molecular Recognition Based on Single-Walled Carbon Nanotube Corona-Phases. *npj Comput. Mater.* **2022**, *8*, 135.
(65) Chen, C.; Wang, W.; Wang, Z.; Wei, F.; Zhao, X. S. Influence of Secondary Structure on Kinetics and Reaction Mechanism of DNA Hybridization. *Nucleic Acids Res.* **2007**, *35*, 2875−2884.
(66) Owczarzy, R.; Tataurov, A. V.; Wu, Y.; Manthey, J. A.; McQuisten, K. A.; Almabrazi, H. G.; Pedersen, K. F.; Lin, Y.; Garretson, J.; et al. IDT SciTools: A Suite for Analysis and Design of Nucleic Acid Oligomers. *Nucleic Acids Res.* **2008**, *36*, W163−W169.
(67) Gong, X.; Park, M.; Parviz, D.; Silmore, K. S.; Gordiichuk, P.; Lew, T. T. S.; Strano, M. S. Single-Particle Tracking for Understanding Polydisperse Nanoparticle Dispersions. *Small* **2019**, *15*, 1901468.
(68) Marky, L. A.; Breslauer, K. J. Calculating Thermodynamic Data for Transitions of Any Molecularity from Equilibrium Melting Curves. *Biopolymers* **1987**, *26*, 1601−1620.
(69) Wu, P.; Sugimoto, N. Transition Characteristics and Thermodynamic Analysis of DNA Duplex Formation: A Quantitative Consideration for the Extent of Duplex Association. *Nucleic Acids Res.* **2000**, *28*, 4762−4768.
(70) Dimitrov, R. A.; Zuker, M. Prediction of Hybridization and Melting for Double-Stranded Nucleic Acids. *Biophys. J.* **2004**, *87*, 215−226.
(71) SantaLucia, S. A Unified View of Polymer, Dumbbell, and Oligonucleotide DNA Nearest-Neighbor Thermodynamics. *Proc. Natl. Acad. Sci. U.S.A.* **1998**, *95*, 1460−1465.
(72) Bisker, G.; Dong, J.; Park, H. D.; Iverson, N. M.; Ahn, J.; Nelson, J. T.; Landry, M. P.; Kruss, S.; Strano, M. S. Protein-Targeted Corona Phase Molecular Recognition. *Nat. Commun.* **2016**, *7*, 10241.
(73) Heller, D. A.; Jeng, E. S.; Yeung, T.-K.; Martinez, B. M.; Moll, A. E.; Gastala, J. B.; Strano, M. S. Optical Detection of DNA Conformational Polymorphism on Single-Walled Carbon Nanotubes. *Science* **2006**, *311*, 508−511.
(74) Park, M.; Salem, D. P.; Parviz, D.; Gong, X.; Silmore, K. S.; Lew, T. T. S.; Khong, D. T.; Ang, M. C.-Y.; Kwak, S.-Y.; et al. Measuring the Accessible Surface Area within the Nanoparticle Corona Using Molecular Probe Adsorption. *Nano Lett.* **2019**, *19*, 7712−7724.
(75) Iliafar, S.; Mittal, J.; Vezenov, D.; Jagota, A. Interaction of Single-Stranded DNA with Curved Carbon Nanotube Is Much Stronger Than with Flat Graphite. *J. Am. Chem. Soc.* **2014**, *136*, 12947−12957.
(76) Das, A.; Sood, A. K.; Maiti, P. K.; Das, M.; Varadarajan, R.; Rao, C. N. R. Binding of Nucleobases with Single-Walled Carbon Nanotubes: Theory and Experiment. *Chem. Phys. Lett.* **2008**, *453*, 266−273.
(77) Akdim, B.; Pachter, R.; Day, P. N.; Kim, S. S.; Naik, R. R. On Modeling Biomolecular−Surface Nonbonded Interactions: Application to Nucleobase Adsorption on Single-Wall Carbon Nanotube Surfaces. *Nanotechnology* **2012**, *23*, 165703.
(78) Wang, Y. Theoretical Evidence for the Stronger Ability of Thymine to Disperse SWCNT than Cytosine and Adenine: Self-Stacking of DNA Bases vs Their Cross-Stacking with SWCNT. *J. Phys. Chem. C* **2008**, *112*, 14297−14305.
(79) Priya, B. R.; Byrne, H. J. Investigation of Sodium Dodecyl Benzene Sulfonate Assisted Dispersion and Debundling of Single-Wall Carbon Nanotubes. *J. Phys. Chem. C* **2008**, *112*, 332−337.
(80) Richard, C.; Balavoine, F.; Schultz, P.; Ebbesen, T. W.; Mioskowski, C. Supramolecular Self-Assembly of Lipid Derivatives on Carbon Nanotubes. *Science* **2003**, *300*, 775−778.
(81) Islam, M. F.; Rojas, E.; Bergey, D. M.; Johnson, A. T.; Yodh, A. G. High Weight Fraction Surfactant Solubilization of Single-Wall Carbon Nanotubes in Water. *Nano Lett.* **2003**, *3*, 269−273.
(82) Wetmur, J. G.; Davidson, N. Kinetics of Renaturation of DNA. *J. Mol. Biol.* **1968**, *31*, 349−370.
(83) Bishop, J.; Blair, S.; Chagovetz, A. M. A Competitive Kinetic Model of Nucleic Acid Surface Hybridization in the Presence of Point Mutants. *Biophys. J.* **2006**, *90*, 831−840.
(84) Halperin, A.; Buhot, A.; Zhulina, E. B. On the Hybridization Isotherms of DNA Microarrays: The Langmuir Model and Its Extensions. *J. Phys.: Condens. Matter* **2006**, *18*, S463.
(85) Teo, A. K. J.; Choudhury, Y.; Tan, I. B.; Cher, C. Y.; Chew, S. H.; Wan, Z. Y.; Cheng, L. T. E.; Oon, L. L. E.; Tan, M. H.; et al. Saliva Is More Sensitive than Nasopharyngeal or Nasal Swabs for Diagnosis of Asymptomatic and Mild COVID-19 Infection. *Sci. Rep.* **2021**, *11*, 3134.
(86) Kubala, E.; Strzelecka, P.; Grzegocka, M.; Lietz-Kijak, D.; Gronwald, H.; Skomro, P.; Kijak, E. A Review of Selected Studies That Determine the Physical and Chemical Properties of Saliva in the Field of Dental Treatment. *BioMed Res. Int.* **2018**, *2018*, 6572381.
(87) Ngamchuea, K.; Batchelor-McAuley, C.; Compton, R. G. The Fate of Silver Nanoparticles in Authentic Human Saliva. *Nanotoxicology* **2018**, *12*, 305−311.
(88) Cho, S.-Y.; Jin, X.; Gong, X.; Yang, S.; Cui, J.; Strano, M. S. Antibody-Free Rapid Detection of SARS-CoV-2 Proteins Using Corona Phase Molecular Recognition to Accelerate Development Time. *Anal. Chem.* **2021**, *93*, 14685−14693.
(89) To, K. K.-W.; Tsang, O. T.-Y.; Leung, W.-S.; Tam, A. R.; Wu, T.-C.; Lung, D. C.; Yip, C. C.-Y.; Cai, J.-P.; Chan, J. M.-C.; et al.

https://doi.org/10.1021/acs.jpcc.2c06434
J. Phys. Chem. C 2023, 127, 606−620

Temporal Profiles of Viral Load in Posterior Oropharyngeal Saliva Samples and Serum Antibody Responses during Infection by SARS-CoV-2: An Observational Cohort Study. *Lancet Infect. Dis.* **2020**, *20*, 565−574.

(90) Sahoo, P. R.; Sethy, K.; Mohapatra, S.; Panda, D. Loop Mediated Isothermal Amplification: An Innovative Gene Amplification Technique for Animal Diseases. *Vet. World* **2016**, *9*, 465−469.

https://doi.org/10.1021/acs.jpcc.2c06434
J. Phys. Chem. C 2023, 127, 606−620